Supplementary materials

Indications of Ferroelectric Behaviour Near Room Temperature in the Organic–Inorganic Hybrid Q_2CuBr_4

Agnieszka Cizman[1], Dorota A. Kowalska[2], Paweł Szarek[3], Wojciech Medycki[4], Natalia Anna Wójcik[5], Marek Gusowski[1], Monika Trzebiatowska[2], Adam Bartosiewicz[1], Ludmila Filevskaya[1], Piotr Staniorowski[5], Ewelina Jach[1]

[1] Wrocław University of Science and Technology, Department of Experimental Physics, 27 Wybrzeże Wyspiańskiego, 50-370 Wrocław, Poland

[2] Institute of Low Temperature and Structure Research, Polish Academy of Sciences, Okólna 2, 50-422 Wrocław, Poland

[3] Navi-Chem, Włodarzewska 83/120, Warsaw, Poland

[4] Institute of Molecular Physics, Polish Academy of Science, M. Smoluchowskiego 17, 60-179 Poznań, Poland

[5] Institute of Nanotechnology and Material Engineering, Gdansk University of Technology, Narutowicza 11/12, 80-233 Gdansk, Poland

[6] Institute of Experimental Physics, University of Wrocław, Pl. M. Borna 9, 50204 Wrocław, Poland

Table content

Table S8. The fundamental, $I - A$, and optical, $\epsilon_L - \epsilon_H = min(\epsilon_{LUMO}^{\alpha}, \epsilon_{LUMO}^{\beta}) - max(\epsilon_{HOMO}^{\alpha}, \epsilon_{HOMO}^{\beta})$, gaps in eV, at different levels of theory: non-relativistic, relativistic DKH, and DKHSO, for crystallographic unit cell in high spin – quintet, and low spin – antiferromagnetic singlet states.

Table S9. Dipole moments in Debye, of unit cell structures. The DKH, $\sum \mu_i$ are resultant dipole moments of four dipoles of isolated sub-units, of the unit cell, summed together.

Table S10. Polarizability, α, and first hyperpolarizability, β, in atomic units, of unit cell structures. For reference the hyperpolarizability of urea is 37.

Table S11. Average chemical shifts in ppm between corresponding atoms in unit cells in high spin quintet state and in low spin antiferromagnetic singlet states.

Table S12. The wavenumbers (cm^{-1}) of the observed infrared bands of Q_2CuBr_4 at 300 K and their assignment.

Graph content

Figure S1. Comparison of measured powder X-ray diffraction data with calculated pattern

Figure S2. The asymmetric unit of the Q_2CuBr_4 with atom numbering scheme: (a) ordered phase II at 100 K and (b) phase II at 300 K with disordered Q2 cation (presented in transparent color and with dashed bonds). The N—H···Br bonds are presented as green dashed lines.

Figure S3. The view at the Q_2CuBr_4 structure along the *b*-crystallographic direction in phase II (a) and phase I (b). The Q ions are presented in two different colors to differentiate the Q2 moiety (in pink) from the Q1 (in grey). The disordered cations in (b) are presented with dotted pink lines. For the picture clarity the hydrogen atoms attached to carbon atoms were removed. The N—H···Br bonds are presented as green dashed lines.

Figure S4. The volume changes (a) and relative changes of lattice parameters (b) around PT for Q_2CuBr_4 derived from X-ray diffraction measurements.

Figure S5. The temperature dependence of (a) the third-order conductivity coefficient, (b) the real part of the third-order electric susceptibility coefficient measured at frequency of 1 Hz during heating and cooling.

Figure S6. Aligned structures of Q_2CuBr_4 sub-unit from 100 K (green), two conformers in 300 K (blue and yellow) and geometries optimized with different functionals (grey).

Figure S7. Comparison of relative energies of neutral and charged species of low and high temperature single cell structures, ionization potential, IP, and electron affinity, EA, at different levels of theory: non-relativistic and relativistic DKH and DKHSO.

Figure S8. The IR spectra of Q_2CuBr_4.

Table S1. Selected hydrogen bond parameters.

Phase (temp.)	*D*—H···*A*	*D*—H (Å)	H···*A* (Å)	*D*···*A* (Å)	*D*—H···*A* (°)
Phase II (100 K)	N1—H1···Br2	0.98	2.45	3.359(3)	154
	N2—H2···Br1	0.98	2.41	3.326(4)	155
	N3—H3···Br5	0.98	2.46	3.330(4)	148
	N4—H4···Br6	0.98	2.45	3.338(4)	151
Phase I (300 K)	N1—H1···Br2	0.98	2.51	3.409(5)	153
	N2—H2···Br1	1.00(2)	2.43(3)	3.363(5)	155(5)

Table S2. Selected geometric parameters (Å, °) of inorganic polyhedra in Q_2CuBr_4.

Phase (temp.)	Bond	Bond length (Å)	Angle description	Angle value (°)
Phase II (100 K)	Cu1—Br1	2.4124(8)	Br2—Cu1—Br1	133.37(3)
	Cu1—Br2	2.3857(9)	Br2—Cu1—Br3	98.64(3)
	Cu1—Br3	2.3986(8)	Br3—Cu1—Br1	98.49(3)
	Cu1—Br4	2.3699(8)	Br4—Cu1—Br1	99.04(2)
	Cu2—Br5	2.3996(8)	Br4—Cu1—Br2	101.57(3)
	Cu2—Br6	2.3794(8)	Br4—Cu1—Br3	131.00(3)
	Cu2—Br7	2.4115(8)	Br5—Cu2—Br7	98.79(3)
	Cu2—Br8	2.3626(8)	Br6—Cu2—Br5	133.65(3)
			Br6—Cu2—Br7	100.25(3)
			Br8—Cu2—Br5	99.27(3)
			Br8—Cu2—Br6	100.53(3)
			Br8—Cu2—Br7	129.21(3)
Phase I (300 K)	Cu1—Br1	2.3998(18)	Br2—Cu1—Br1	132.68(3)
	Cu1—Br2	2.3815(18)	Br2—Cu1—Br3	99.65(3)
	Cu1—Br3	2.3935(17)	Br3—Cu1—Br1	99.06(3)
	Cu1—Br4	2.3602(18)	Br4—Cu1—Br1	99.02(3)
			Br4—Cu1—Br2	101.76(3)
			Br4—Cu1—Br3	129.38(4)

Table S3. Properties of single Q_2CuBr_4 sub-unit, depending on functional, Jorge-DZP-DKH basis set and scalar relativistic correction. Kohn-Sham energies in Hartree. The vertical ionization energy, *I*,

vertical electron affinity, A, $I-A$ estimated by finite differences, $E_{N+1}+E_{N-1}-2E_N$, and the $gap = min(\epsilon^{\alpha}_{LUMO},\epsilon^{\beta}_{LUMO}) - max(\epsilon^{\alpha}_{HOMO},\epsilon^{\beta}_{HOMO})$.

$Structure$	$E\,[eV]$	$I\,[eV]$	$A\,[eV]$	$\alpha HOMO$	$\alpha LUMO$	$\beta HOMO$	$\beta LUMO$	$I-A$	$gap[eV]$
				B97D					
optimized	0.000	6.802	1.297	-0.1705	-0.0110	-0.1650	-0.1485	5.506	0.450
100K	11.328	5.885	-0.028	-0.1295	0.0072	-0.1264	-0.1051	5.840	0.580
300K v1	11.926	5.885	-0.086	-0.1280	0.0060	-0.1240	-0.1035	5.891	0.559
300K v2	11.958	5.867	-0.088	-0.1274	0.0061	-0.1233	-0.1028	5.876	0.559
				M06					
optimized	0.000	7.121	1.369	-0.2145	0.0150	-0.2116	-0.1119	5.751	2.713
100K	10.683	6.326	0.178	-0.1823	0.0305	-0.1789	-0.0742	6.077	2.848
300K v1	11.095	6.294	0.118	-0.1812	0.0289	-0.1781	-0.0725	6.104	2.872
300K v2	11.157	6.277	0.094	-0.1805	0.0289	-0.1773	-0.0717	6.109	2.874
				M06L					
optimized	0.000	6.773	1.061	-0.1763	0.0117	-0.1678	-0.1403	5.713	0.749
100K	10.343	5.895	-0.326	-0.1366	0.0304	-0.1324	-0.0961	6.221	0.986
300K v1	10.788	5.900	-0.388	-0.1352	0.0327	-0.1302	-0.0944	6.288	0.972
300K v2	10.846	5.838	-0.407	-0.1346	0.0324	-0.1295	-0.0937	6.246	0.973
				LC-TPSSTPSS					
optimized	0.000	8.184	1.611	-0.3271	0.0984	-0.3236	-0.0359	6.573	7.828
100K	10.417	7.430	0.623	-0.2983	0.1093	-0.2933	-0.0053	6.806	7.837
300K v1	10.626	7.400	0.553	-0.2974	0.1072	-0.2925	-0.0030	6.847	7.880
300K v2	10.708	7.382	0.531	-0.2967	0.1073	-0.2918	-0.0022	6.851	7.879
				wB97XD					
optimized	0.000	7.602	1.340	-0.2869	0.0831	-0.2811	-0.0533	6.263	6.198
100K	10.521	6.795	0.138	-0.2520	0.1006	-0.2473	-0.0130	6.657	6.377
300K v1	10.981	6.759	0.072	-0.2513	0.0988	-0.2466	-0.0109	6.688	6.414
300K v2	11.037	6.742	0.049	-0.2506	0.0988	-0.2459	-0.0102	6.693	6.415

Table S4. Polarizability, α, and first hiperpolarizability, β, in atomic units, for single Q_2CuBr_4 sub-unit, depending on functional, Jorge-DZP-DKH basis set and DKH relativistic correction.

$Structure$	α	β_x	β_y	β_z	$\beta_{\parallel}$	β_{vec}	$cos\theta$	β_{tot}
				B97D				
opt	280.70	-1368.3	255.0	1477.2	1217.8	1598.3	0.7875	2029.6
100K	246.26	-1534.1	-815.0	1067.5	1223.4	1955.5	0.9591	2038.9
300K v1	244.57	-1545.7	-890.9	1100.2	1257.6	2009.2	0.9585	2096.1
300K v2	244.67	-1547.6	-899.4	1038.3	1241.6	1997.1	0.9651	2069.3
				M06				
opt	264.50	-971.5	478.3	1153.6	949.3	1080.6	0.6830	1582.2
100K	236.45	-1014.8	-589.4	1103.8	966.6	1425.4	0.8848	1611.1
300K v1	234.12	-976.6	-642.4	1146.7	982.5	1432.7	0.8750	1637.5
300K v2	234.02	-968.4	-630.2	1092.1	953.9	1408.5	0.8859	1589.8
				M06L				
opt	266.70	-1214.8	513.1	1205.1	1071.9	1261.1	0.7059	1786.5

100K	232.08	-1030.1	-675.0	1137.3	1005.8	1479.2	0.8824	1676.3
300K v1	230.02	-1026.4	-739.5	1173.6	1035.3	1518.9	0.8803	1725.5
300K v2	229.92	-1009.8	-725.8	1096.9	994.9	1479.7	0.8923	1658.2
LC-TPSSTPSS								
opt	234.28	-1164.8	-67.0	552.6	774.6	1225.9	0.9495	1291.0
100K	213.90	-1242.9	-380.8	697.2	885.1	1439.7	0.9760	1475.1
300K v1	211.53	-1165.8	-366.0	707.0	847.0	1373.8	0.9731	1411.7
300K v2	211.68	-1168.5	-339.8	678.8	836.0	1360.9	0.9767	1393.4
wB97XD								
opt	251.08	-1119.6	256.0	964.9	900.0	1253.6	0.8358	1500.0
100K	222.78	-1164.9	-507.5	826.0	909.3	1449.4	0.9564	1515.5
300K v1	220.52	-1133.3	-514.1	827.9	896.8	1430.2	0.9569	1494.7
300K v2	220.62	-1130.0	-494.5	790.7	879.1	1411.5	0.9634	1465.1

Table S5. Dipole moments in Debye for single Q_2CuBr_4 sub-unit, depending on functional, Jorge-DZP-DKH basis set and DKH relativistic correction.

Structure	μ_x	μ_y	μ_z	μ	$\frac{\mu_x}{\mu}$	$\frac{\mu_y}{\mu}$	$\frac{\mu_z}{\mu}$
B97D							
opt	-8.80	-3.12	3.00	9.81	-89.7%	-31.8%	30.6%
100K	-13.24	-5.17	4.15	14.80	-89.4%	-34.9%	28.0%
300K v1	-12.96	-4.98	4.30	14.54	-89.2%	-34.3%	29.6%
300K v2	-13.10	-4.96	4.45	14.70	-89.1%	-33.7%	30.3%
M06							
opt	-9.25	-3.03	3.01	10.18	-90.8%	-29.7%	29.5%
100K	-13.57	-5.34	4.31	15.21	-89.2%	-35.1%	28.3%
300K v1	-13.29	-5.16	4.45	14.94	-89.0%	-34.5%	29.8%
300K v2	-13.45	-5.13	4.60	15.11	-89.0%	-33.9%	30.5%
M06L							
opt	-9.54	-3.66	3.13	10.69	-89.3%	-34.3%	29.3%
100K	-13.78	-5.40	4.39	15.44	-89.3%	-35.0%	28.5%
300K v1	-13.51	-5.21	4.54	15.18	-89.0%	-34.3%	29.9%
300K v2	-13.65	-5.19	4.69	15.34	-89.0%	-33.8%	30.6%
LC-TPSSTPSS							
opt	-9.39	-3.60	3.14	10.53	-89.1%	-34.2%	29.9%
100K	-14.15	-5.50	4.42	15.82	-89.5%	-34.8%	28.0%
300K v1	-13.87	-5.28	4.57	15.53	-89.3%	-34.0%	29.4%
300K v2	-14.03	-5.25	4.69	15.70	-89.4%	-33.4%	29.9%
wB97XD							
opt	-9.78	-2.81	3.30	10.69	-91.4%	-26.3%	30.8%
100K	-13.92	-5.41	4.33	15.55	-89.5%	-34.8%	27.8%
300K v1	-13.64	-5.20	4.48	15.27	-89.3%	-34.0%	29.3%
300K v2	-13.80	-5.17	4.61	15.44	-89.4%	-33.5%	29.9%

Table S6. Relative energies in eV, of high and low temperature single cell structures with triple-ζ basis set quality (Jorge-TZP and Jorge-TZP-DKH combined with LC-TPSSTPSS).

	non-relat.	**DKH**	**DKHSO**
100K	0.000	0.000	0.000
300K v1	1.043	1.030	1.030
300K v2	1.318	1.305	1.305

Table S7. Relative energies of high spin – quintet states for single unit cell structures at different levels of theory (Jorge-DZP and Jorge-DZP-DKH combined with LC-TPSSTPSS).

	E_{N+1}	E_N	E_{N-1}	I	A
			100K		
non-relat.	-1.573	0.000	7.319	7.319	1.573
DKH	-1.357	0.000	7.530	7.530	1.357
DKHSO	-1.357	0.000	7.528	7.528	1.357
			300K v1		
non-relat.	-0.364	1.170	8.466	7.296	1.534
DKH	-0.171	1.121	8.334	7.213	1.293
DKHSO	-0.171	1.121	8.333	7.211	1.293
			300K v2		
non-relat.	-0.057	1.454	8.752	7.298	1.511
DKH	0.135	1.405	8.963	7.557	1.271
DKHSO	0.135	1.405	8.961	7.556	1.271

Table S8. The fundamental, $I - A$, and optical, $\epsilon_L - \epsilon_H = min(\epsilon_{LUMO}^{\alpha}, \epsilon_{LUMO}^{\beta}) - max(\epsilon_{HOMO}^{\alpha}, \epsilon_{HOMO}^{\beta})$, gaps in eV, at different levels of theory: non-relativistic, relativistic DKH, and DKHSO, for crystallographic unit cell in high spin – quintet, and low spin – antiferromagnetic singlet states.

	Non-relatativistic		**DKH**		**DKHSO**	
	$I - A$	$\epsilon_L - \epsilon_H$	$I - A$	$\epsilon_L - \epsilon_H$	$I - A$	$\epsilon_L - \epsilon_H$
			100K			
high spin	5.746	7.143	6.173	7.306	6.171	7.305
low spin	—	—	5.897	7.306	—	—
			300K v1			
high spin	5.763	7.157	5.920	7.329	5.918	7.328
low spin	—	—	5.920	7.329	—	—
			300K v2			
high spin	5.786	7.184	6.286	7.354	6.285	7.353
low spin	—	—	5.943	7.354	—	—

Table S9. Dipole moments in Debye, of unit cell structures. The DKH, $\sum \mu_i$ are resultant dipole moments of four dipoles of isolated sub-units, of the unit cell, summed together.

Structure	μ_x	μ_y	μ_z	μ
		non-relativistic		
100K	0.347	-1.47	1.07	1.86
300K v1	1.11	-1.65	1.08	2.26
300K v2	1.15	-1.69	1.05	2.29
		DKH		
100K	0.361	-1.49	1.08	1.88
300K v1	1.11	-1.66	1.08	2.27
300K v2	1.15	-1.70	1.04	2.30
		DKHSO		
100K	0.361	-1.49	1.08	1.88
300K v1	1.11	-1.66	1.08	2.27
300K v2	1.15	-1.70	1.04	2.30
		DHK, $\sum \mu_i$		
100K	-0.910	0.000	-0.268	0.948
300K v1	0.000	0.000	0.000	0.000
300K v2	0.000	0.000	0.000	0.000

Table S10. Polarizability, α, and first hyperpolarizability, β, in atomic units, of unit cell structures. For reference the hyperpolarizability of urea is 37.

Structure	α	β_x	β_y	β_z	$\beta_{\parallel}$	β_{vec}	$cos\theta$	β_{tot}
				non-relativistic				
100K	881.24	219.55	691.91	-37.56	436.13	-530.17	-0.7294	726.88
300K v1	868.31	443.43	604.66	-66.74	451.68	-255.24	-0.3391	752.79
300K v2	869.63	444.02	628.88	-43.18	462.63	-259.83	-0.3370	771.05
				DKH				
100K	877.12	182.32	561.03	-101.78	359.17	-470.03	-0.7852	598.62
300K v1	864.26	346.36	526.44	-128.94	385.93	-276.59	-0.4300	643.22
300K v2	865.57	348.26	554.79	-110.70	398.60	-285.70	-0.4301	664.33
				DKHSO				
100K	877.35	182.27	561.65	-101.73	359.51	-470.50	-0.7852	599.18
300K v1	864.49	346.74	526.75	-128.74	386.18	-276.53	-0.4296	643.64
300K v2	865.80	348.67	555.11	-110.47	398.86	-285.62	-0.4297	664.77

Table S11. Average chemical shifts in ppm between corresponding atoms in unit cells in high spin quintet state and in low spin antiferromagnetic singlet states.

	100K	**300K v1**	**300K v2**
Br	13.54	12.48	12.56
Cu	-10.58	-10.86	-10.82
N	0.159	0.155	0.151
C	0.130	0.122	0.124
H	0.053	0.052	0.052

Table S12. The wavenumbers (cm^{-1}) of the observed infrared bands of Q_2CuBr_4 at 300 K and their assignment.

IR	**Assignment**
3060vs	νNH νCH $\nu_{as}CH_2$
2964sh	νNH $\nu_{as}CH_2$
2957s	$\nu_{as}CH_2$
2946s	$\nu_{as}CH_2$ ν_sCH_2
2901w	ν_sCH_2
2884m	ν_sCH_2
2829m	$\nu_{as}CH_2$ ν_sCH_2
2752vw	overtone
2679w	combination
2608w	combination
1628vw	γNH
1494m	δCH_2
1488sh	δCH_2
1464s	δCH_2
1422s	γNH δCH_2
1396s	γNH δCH_2
1384m	δCH_2
1342w	ωCH_2
1314m	γCH ωCH_2
1294w	ωCH_2
1265vw	τCH_2
1254vw	τCH_2
1241vw	τCH_2
1189w	ν_{as}CNC ν_{as}CCC
1169vw	ν_{as}CNC ν_{as}CCC
1118w	ν_sCNC ν_sCCC
1039m	ν_sCNC ν_sCCC
1031sh	τCH_2
965m	τCH_2
883w	γNH
839w	γNH
809w	γNH

786vw	ν_sCNC ν_sCCC
775vw	ν_sCNC ν_sCCC
613w	δCNC δCCC

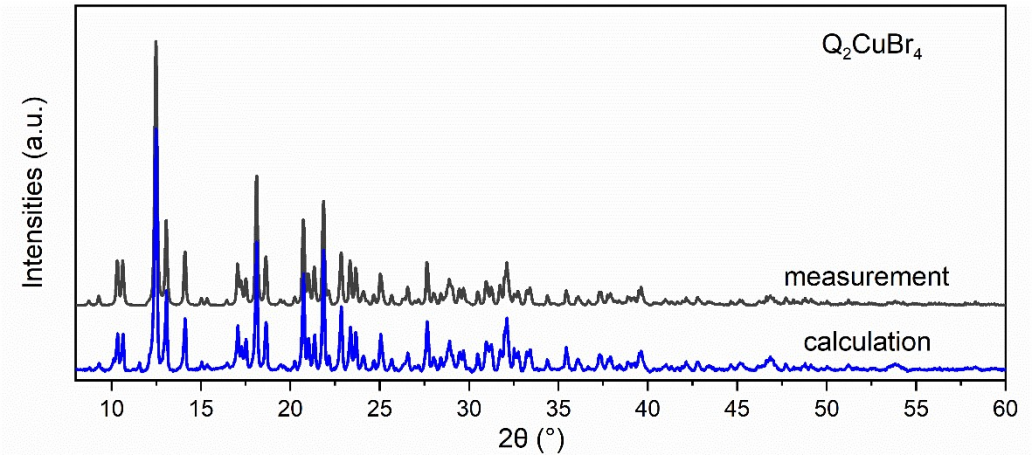

Figure S1. Comparison of measured powder X-ray diffraction data with calculated pattern.

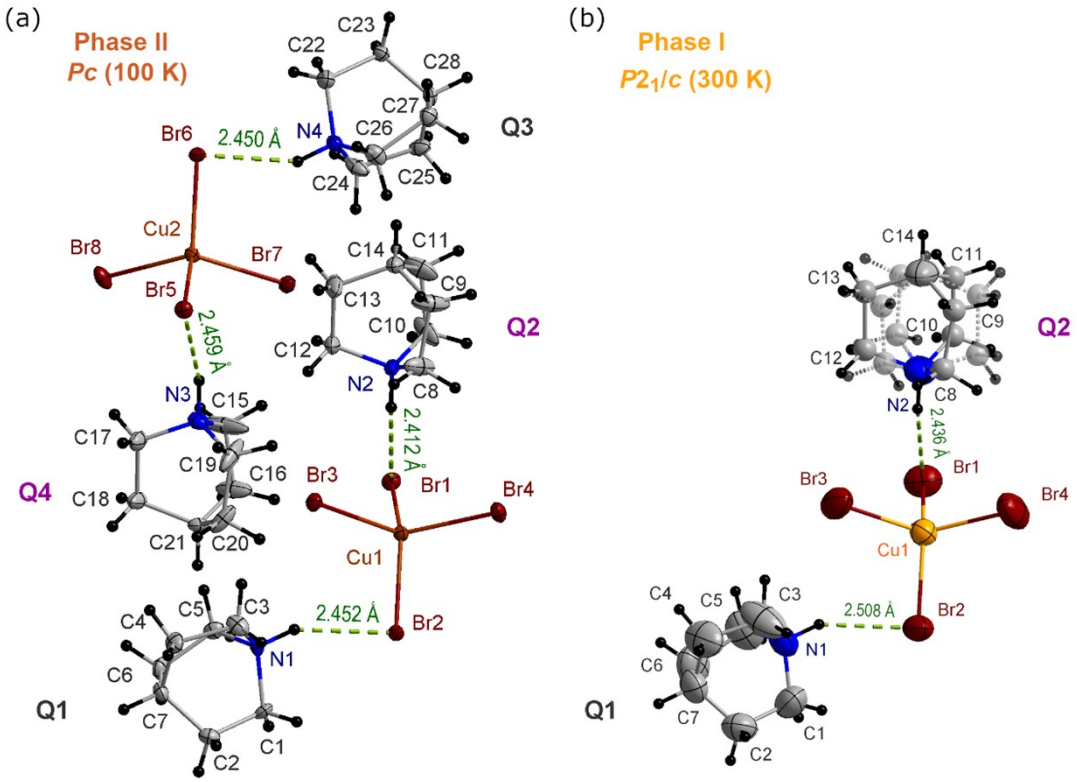

Figure S2. The asymmetric unit of the Q_2CuBr_4 with atom numbering scheme: (a) ordered phase II at 100 K and (b) phase II at 300 K with disordered Q2 cation (presented in transparent color and with dashed bonds). The N—H···Br bonds are presented as green dashed lines.

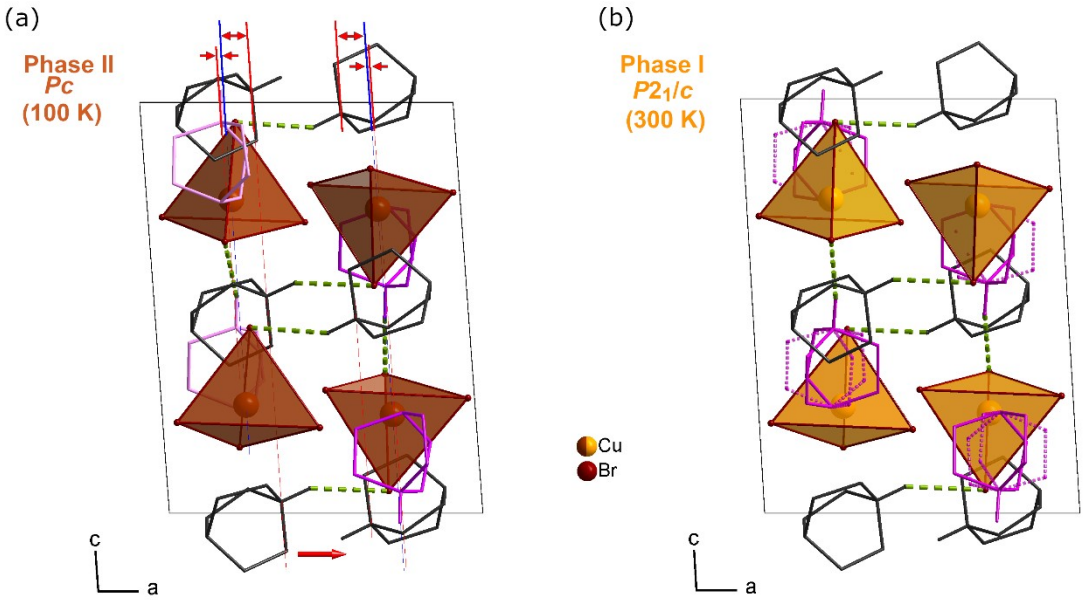

Figure S3. The view at the Q_2CuBr_4 structure along the *b*-crystallographic direction in phase II (a), showing in a schematic way ferroelectric displacement in the *a*-crystallographic direction, and phase I (b). The Q ions are presented in two different colors to differentiate the Q2 moiety (in pink) from the Q1 (in grey). The disordered cations in (b) are presented with dotted pink lines. For the picture clarity the hydrogen atoms attached to carbon atoms were removed. The N—H···Br bonds are presented as green dashed lines.

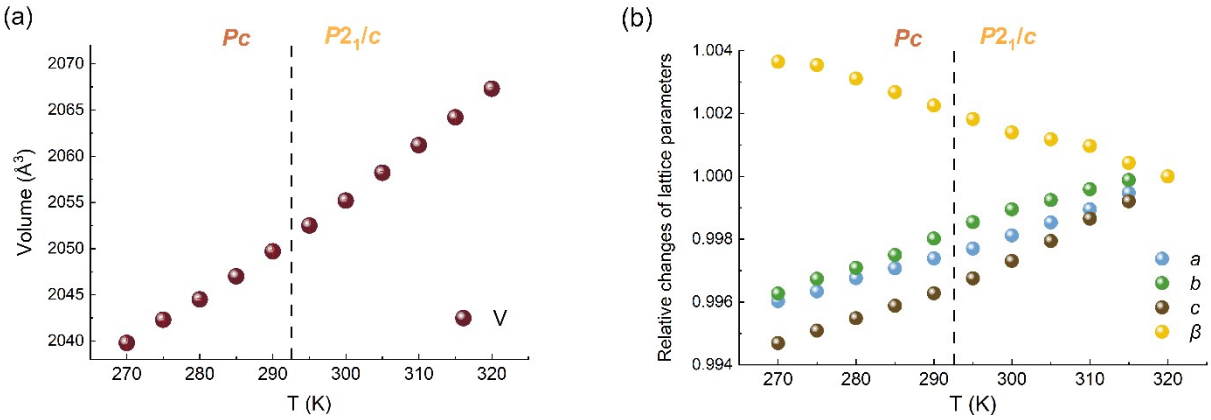

Figure S4. The volume changes (a) and relative changes of lattice parameters (b) around PT for Q_2CuBr_4 derived from X-ray diffraction measurements.

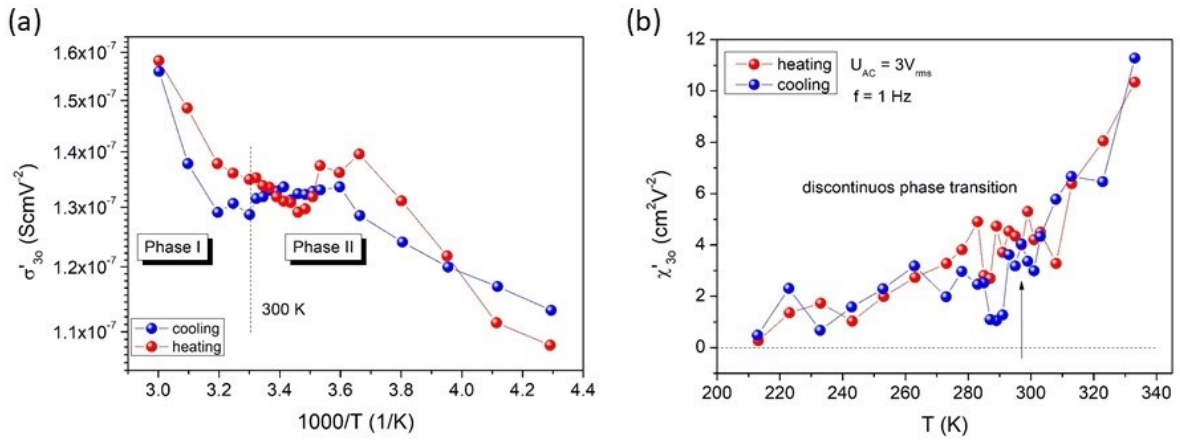

Figure S5. The temperature dependence of (a) the third-order conductivity coefficient and (b) the real part of the third-order electric susceptibility coefficient measured at frequency of 1 Hz during heating and cooling.

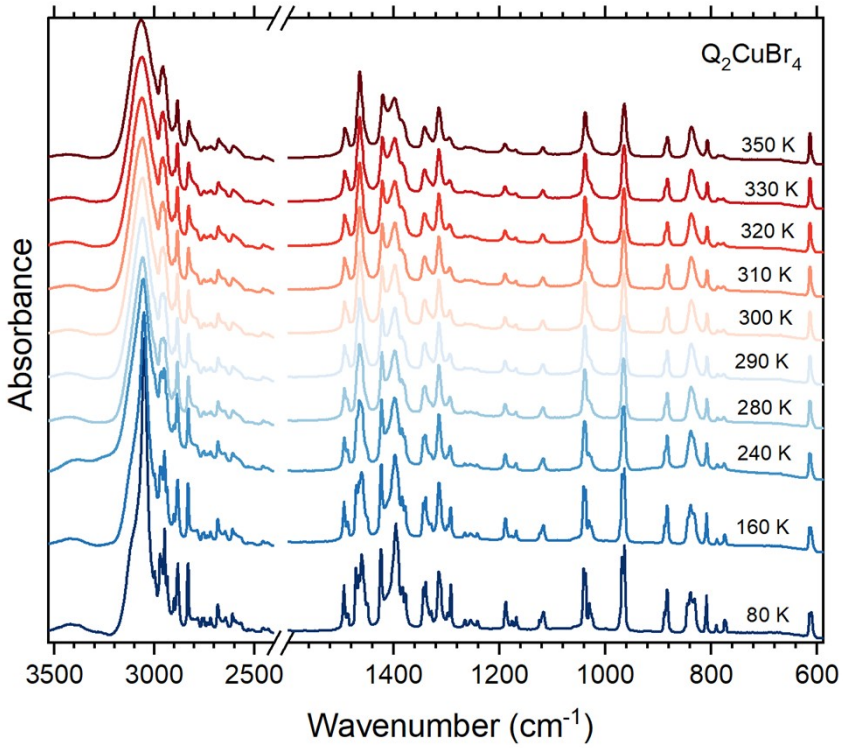

Figure S6. The IR spectra of Q_2CuBr_4.

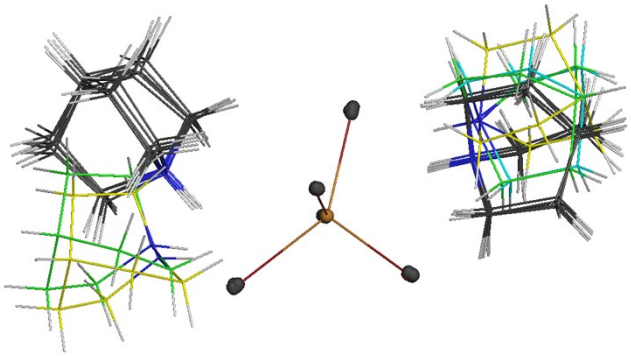

Figure S7. Aligned structures of Q_2CuBr_4 sub-units from 100 K (green), two conformers in 300 K (blue and yellow) and geometries optimized with different functionals (grey).

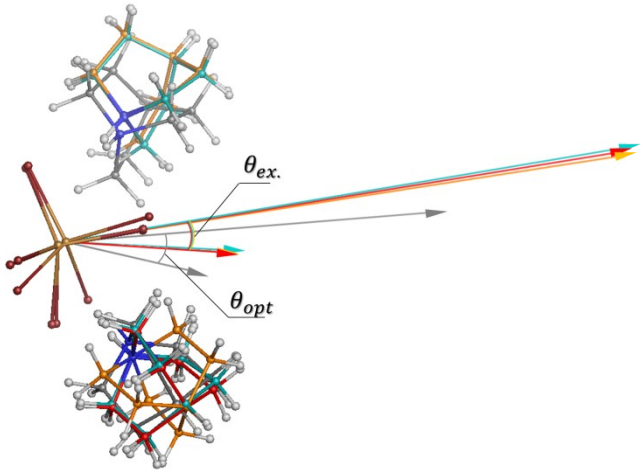

Figure S8. Orientation of electric dipole moment (longer arrows) and first order hiperpolarizablity (short arrows) in LTP (blue), HTP (red, orange) and optimized (grey) structures aligned wrt Cu, N, N atoms.

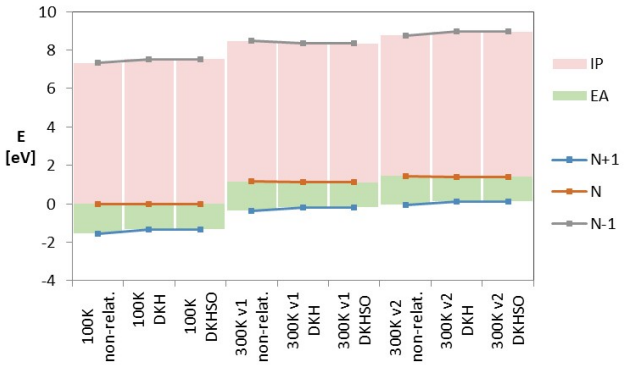

Figure S9. Comparison of relative energies of neutral and charged species for LTP and HTP single cell structures, ionization potential, IP, and electron affinity, EA, at different levels of theory: non-relativistic and relativistic DKH and DKHSO.

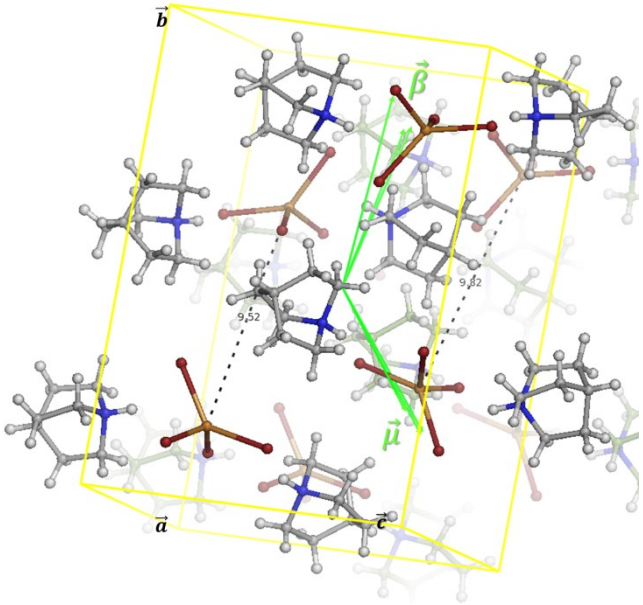

Figure S10. Orientation of first order hiperpolarizability, $\vec{\beta}$, and electric dipole, $\vec{\mu}$, vectors in unit cell. Approximate charge transfer direction is indicated by broken lines connecting Cu ions.

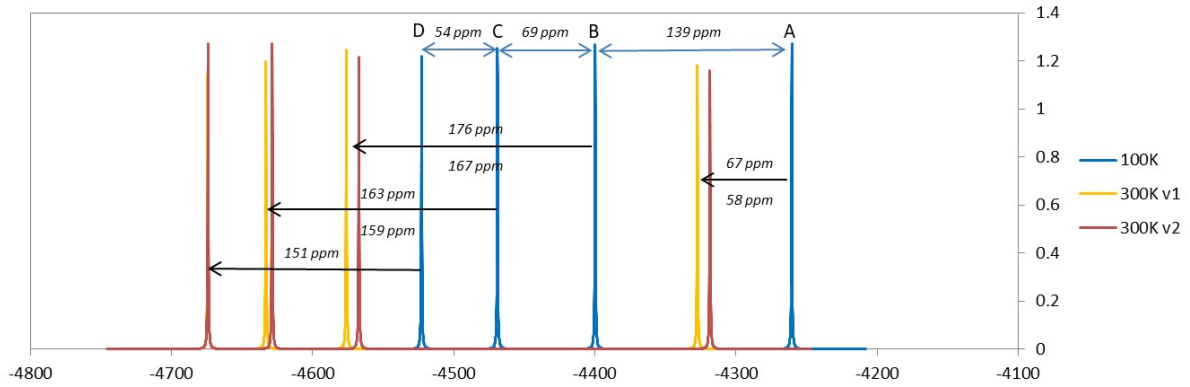

Figure S11. The Cu atoms chemical shifts between four Q_2CuBr_4 sub-units A, B, C and D in a unit cell, and between unit cells of LTP and HPT phases.

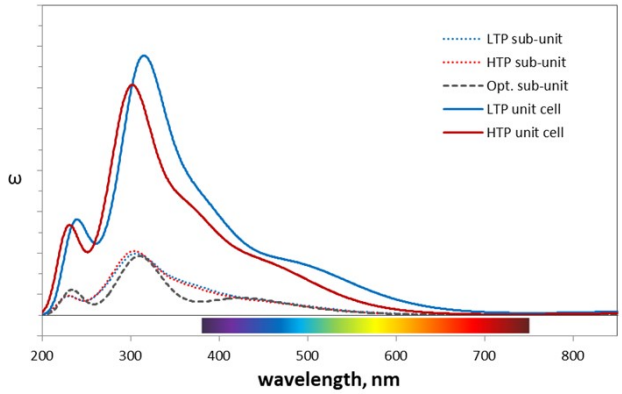

Figure S12. The UV-Vis spectrum calculated for LTP, HTP, and optimized Q_2CuBr_4 sub-units, and LTP and HTP unit cell structures.

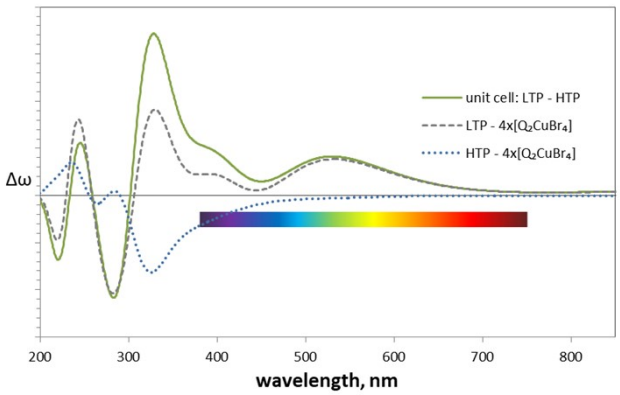

Figure S13. Difference between UV-Vis curves for unit cell LTP structure and unit cell HTP structure, or the unit cell LTP structure and 4 times the sub-unit curves, and the unit cell HTP structure and 4 times the sub-unit curves.

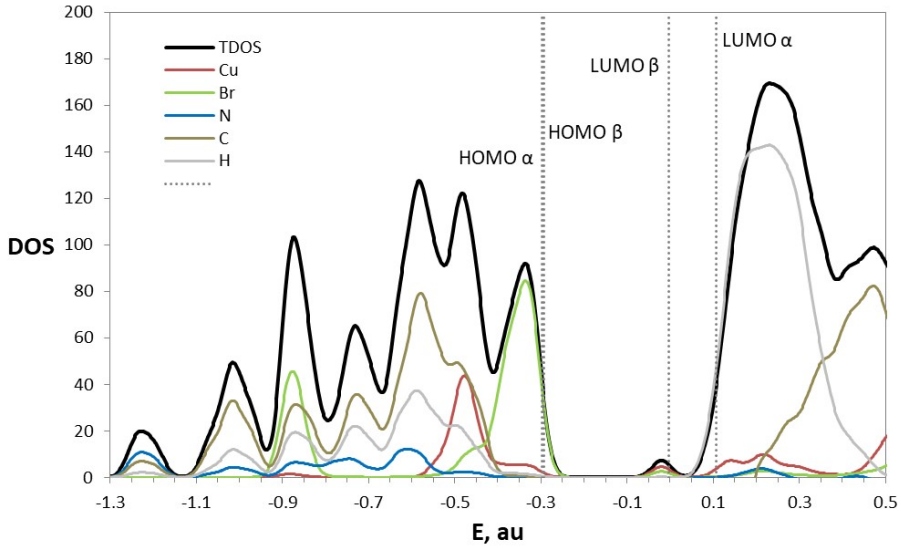

Figure S14. DOS and PDOS calculated in unit cells.

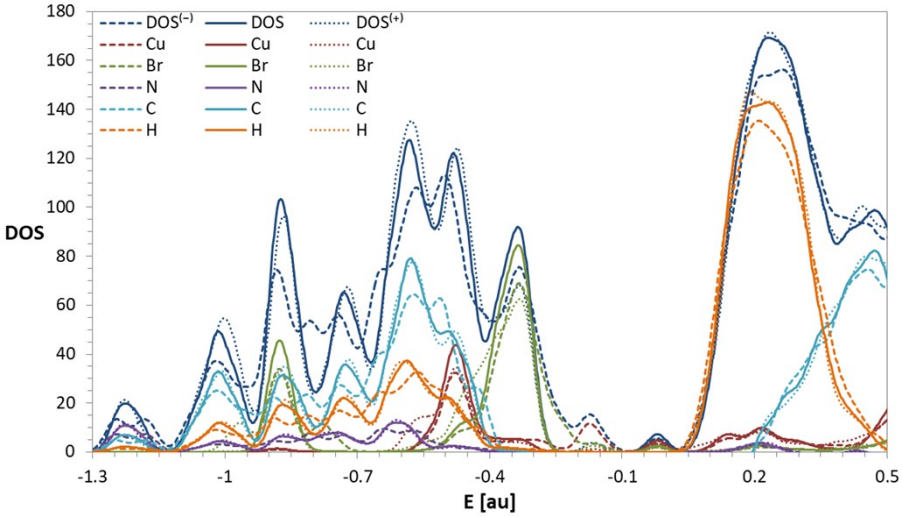

Figure S15. Aligned neutral system DOS, anionic system $DOS^{(-)}$ and cationic system $DOS^{(+)}$

calculated in unit cells.

Theoretical Results

Validation of the Computational Method.

Different conformations of isolated Q_2CuBr_4 sub-unit were modelled in gas phase, at fixed (experimental) and relaxed (optimized) geometries.

Relaxed structures of Q_2CuBr_4 sub-unit are about 10 eV lower in energy than the fixed experimental geometries. The energies are presented in **Table S3**. The energy difference between HTP (phase I) and LTP (phase II) sub-unit structures is about 0.5 eV with B97D, M06, M06L and wB97XD functionals, while with LC-TPSSTPSS it is twice lower.

The B97D, M06 and M06L functionals estimate very low frontier orbital originated gaps ($\epsilon_{LUMO} - \epsilon_{HOMO}$, the optical gap [1]), **Table S3**, as compared to the finite difference values obtained from vertical ionization energy and electron affinity ($I - A$, the fundamental gap). Predicted $I - A$ gap is quite similar for all methods, approximately $5.5 - 6.5$ eV for optimized structures, and $5.8 - 6.8$ eV for experimental geometries, although the optimized structures are about 0.3 eV softer (having a smaller gap). The results for optical gap are more inconclusive, ranging from about 0.5 eV to 7.9 eV depending on the functional chosen. The highest gap values were obtained by the LC-TPSSTPSS and wB97XD functionals, and lower by M06L, M06 and B97D. The LC-TPSSTPSS functional predicts about 1 eV higher optical gaps than the fundamental ones, while wB97XD has optical gaps only about 0.2 eV lower from the fundamental. Optical gaps estimated with remaining functionals are 0.5 - 2.8 eV which is 10% to 50% of the fundamental gap as estimated by respective functional.

Two functionals, namely B97D and M06L, predict negative vertical A. The vertical I are similar among functionals and parallel to fundamental gap. The wB97XD gives the best fit between vertical I and A values and the negative of $max(\epsilon_{HOMO}^{\alpha}, \epsilon_{HOMO}^{\beta})$, and $min(\epsilon_{LUMO}^{\alpha}, \epsilon_{LUMO}^{\beta})$ Khon-Sham orbital eigenvalues, with $I/\epsilon_{HOMO} \cong 1 \pm 0.01$ for all structures and $A/\epsilon_{LUMO} \cong 0.92$ for optimized structure. Second best is LC-TPSSTPSS also with high similarity between estimates. The rest of the functionals has quite different estimates of ionization energy and electron affinity from vertical energies and frontier orbitals. On

account of the inverse relation [2,3] between energy gap and electric dipole polarizability, α, a tendency in the energy gaps might be strengthen, since the lowest α is estimated by LC-TPSSTPSS and wB97XD. For each structure (optimized, LTP and HTP), calculated by different method the fundamental gap correlates with $1/\alpha$. At the same time the M06L functional breaks the trend in case of the optical gap vs. $1/\alpha$. Assuming [3]:

$$I - A \propto \sqrt[3]{\frac{1}{\alpha}} \qquad \text{Eq. S1}$$

the energy gap for sub-units estimated from α is around 4.5 eV (for α refer to **Table S4**).

Besides, the B97D and M06L are less reliable on account of negative electron affinity. The M06L also stands out in correlation between optical gap and polarizability. Moreover the M06, M06L and B97D show considerable mismatch in predicted values of ionization energy and electron affinity form vertical energies and Kohn-Sham "orbital" eigenvalues, with especially unreasonable "optical" electron affinity. This leaves LC-TPSSTPSS and wB97XD, and the greatest difference between two is in optical gap, which is more conservative for the former one.

However the TPSS functional is known for its exceptional performance with respect to predictions of experimental structures [4,5]. Considering the bond lengths and conformation of $CuBr_4^{-2}$ in optimized and experimental structures the LC-TPSSTPSS reproduces very well the experimental geometries. In such case the experimental structures might be viewed as a proxy to ground state structures obtained using LC-TPSSTPSS. The difference in coordination of organic quinuclidine molecules in the isolated optimized Q_2CuBr_4 sub-unit might be explained by lack of interactions (mainly hydrogen bonds) constraining them in the crystal environment, **Figure S7**.

The LC-TPSSTPSS predicts similar orientation of electric dipole moment (wrt surface spanned on Cu, N, N atoms) across aligned different structures - optimized and the experimental LTP and HTP geometries, **Table S5**, and **Figure S8.** Additionally in all cases it shows almost parallel angle ($cos\theta \cong 1$, in **Table S4,** and **Figure S8**) with the first order hyperpolarizability. This indicates that any charge transfer would be approximately parallel or antiparallel to the molecular dipole moment.

Therefore, since in cluster model the fixed experimental geometries are examined, the LC-TPSSTPSS has been selected as the most optimal computational method.

Basis set quality

A single cell structures have been calculated using double-ζ, DZP, and triple-ζ, TZP, basis sets with LC-TPSSTPSS functional, **Tables S6 and S7**. The TZP produce about 8% lower relative energies compared to DZP, yet qualitatively similar results. The energy difference between two HTP variants is almost the same in both basis sets. The energy differences between LTP state and two HTP states in TZP are only less than 0.1 eV smaller as compared with double-ζ basis set. Since there is not much basis set dependence, and due to extensive system size, we deem the Jorge-DZP and Jorge-DZP-DKH basis sets sufficient for system modeling (see **Table S6**).

Energetics and Electronic Structure Characterization

Two variants of HTP unit cell structure are higher in energy from the LTP structure by about 1.12eV and 1.41eV (with relativistic corrections), and by 1.17eV, 1.45eV in non-relativistic limit. Respective results are listed in **Table S7** and compared in **Figure S9**. The HTP structures are therefore thermally excited states of LTP state. The vertical electron affinity is predicted (at relativistic level) approximately 1.3 eV, and vertical ionization potential 7.4 eV, which is quite similar to isolated sub-units, except A is a little higher (calculated with experimental geometries).

Therefore the estimated energy gaps in single unit cell are around 6 eV, presented in **Table S8,** which is similar to aluminum nitride band gap. Because not minimized structures are usually softer than optimized ones the predicted gap may be considered underestimated. However in case of the single Q_2CuBr_4 sub-units the optimized structures actually ended up softer (with a smaller gap) than the fixed geometries based on the crystal structure (**Table S3**). On the other hand in solid state (under periodic conditions) the band gap would get narrower than the values obtained for molecular model (the optical gap reduces in larger systems [6,7]). Moreover the gap estimated from polarizability (**Eq. S1**) in unit cells drops to 2.85 eV, against 4.5 eV in isolated sub-units. Therefore a justified assumption might be made that the real gap of the material is not greater than the estimated 6 eV, and potentially at least week semiconducting properties could be expected.

Electric Properties: Dipole Moment, Polarizability, Hiperpolarizability

The unit cells have small dipole moment of approximately 2 Debye, which originates from the intra-cell interactions between four sub-units, in spite of lack of counter-interactions at unit cell surfaces, **Table**

S9. The sum of dipole moments of four isolated sub-units results in total 0 Debye moments in HTP structures, and in LTP structure the resultant dipole moment of 0.95 D, which is half of the value from the unit cell structure. The intra-cell interactions cause different effect in HTP and LTP structures. The dipole moment in LTP unit cell structure is about 0.4 Debye lower than dipole in HTP unit cell structures. It is mainly driven by μ_x component (uniaxial with the lattice vector 'a'). It might be directly related to quinuclidine bicyclic cage rotation (where one of three N—C bonds aligns parallel to lattice vector "a" on its "positive" or "negative" end). The disparity in dipole moments of two variants of the high temperature phase structures is only 0.03 Debye, and is also associated with ~60° rotation of corresponding but different quinuclidine molecules in the unit cell (one of the two quinuclidine are rotated per each Q_2CuBr_4 sub-unit). Each of the two HTP phase structure variants differ from LTP structure only by two of such rotated quinuclidine molecules.

The isolated Q_2CuBr_4 sub-units have high polarizability, and significant first order hyperpolarizability that is 36 to 40 times higher than in urea [8]. The LC-TPSSTPSS/Jorge-DZP method in gas phase underestimates β for urea by one third, producing 23.54 au ($0.1220 \cdot 10^{-30}$ esu), vs. benchmark value of 37 au ($0.1915 \cdot 10^{-30}$ esu). The calculated polarizability of unit cells is about 4 times higher than that of a single Q_2CuBr_4 sub-unit. Therefore polarizability is approximately "additive" or scalable, which is typical for conducting materials like ionic liquids [9-12]. The first hyperpolarizabilities, β, on the other hand become reduced by half in the unit cell as compared to isolated sub-units, but still it is over 17 or 20 times higher than in urea (for HTP and LTP structures respectively). As indicated by the $cos\theta$ the possible charge transfer direction in LTP structure is relatively antiparallel to the dipole moment vector (~ 140°, which in terms of unit cell parameters - lattice vectors, is $\vec{\beta} \cong [19a,\ 33b,\ -8c]$), while in HTP structures it is more perpendicular to the dipole moment (~ 115°, $\vec{\beta} \cong [36a,\ 31b,\ -9c]$). In both cases it is a direction normal to the surface formed by Cu and two N atoms in Q_2CuBr_4 sub-unit, and along respective line made by Cu ions in the crystal structure, **Figure S10**. In isolated sub-units, the charge transfer direction is almost parallel (~ 12°) with Q_2CuBr_4 dipole moment. Since the LTP structure exhibits the intrinsic non-centrosymmetry, together with non-zero dipole

moment and large first-order hyperpolarizability values, therefore the NLO behavior might be anticipated.

Theoretical NMR Chemical Shifts

It has been shown in the literature that LC-TPSSTPSS functional performs well for chemical shifts. [5,13] The theoretical chemical shifts between high-spin quintet state and low-spin antiferromagnetic singlet states have been compared for LTP and HTP unit cells. The N, C, H atoms show small (< 0.2 ppm) on average, upfield shifts for singlet states as compared to quintet state (summary in **Table S11**). The Br atoms are also upfield shifted, on average by 13.5 ppm or 12.5 ppm (singlet-quintet transition) for LTP and HTP phase structures respectively (the standard deviation among Br atoms is 2.9 ppm). The Cu atoms are downfield shifted, on average by -10.6 ppm or -10.8 ppm in LTP and HTP respectively, with standard deviation of 0.55 ppm.

The shifts between the LTP and the HTP structures are very similar in each spin configuration. The upfield shift for Cu atoms in HTP structures has been observed wrt LTP structure. The magnitude of shifts is different for Cu atom of each Q_2CuBr_4 sub-unit, **Figure S11**. The Cu atoms in sub-units A and C are aligned with the charge transfer direction, with absolute shifts of about 62 ppm and 161 ppm respectively. The Cu in sub-units B and D, with absolute shifts of 171 and 151, are also align along CT direction in the cristal, but not within a single unit cell. Generally downfield shift occurs for N, Br and C atoms, except for few carbon atoms on the rotating quinuclidine ligands.

UV-Vis spectrum

The simulated UV-Vis spectrum, **Figure S12**, shows that photon absorption takes place mainly in the UV region of the spectrum. Around the orange / red region a minimum appears followed by a low flat maximum in the near IR region. The intensity for unit cell curve is approximately 4 times greater than that of a single sub-unit. The LTP structure curve is red-shifted wrt HTP by about 5-8 nm, it has also a greater intensity in orange / red region. The absorption changes between HTP and LTP phase, resulting in maximum difference around the green and violet regions. **Figure S13** shows difference between curves for unit cell structures LTP or HTP and the sum of respective individual isolated sub-units curves. The spectrum does not change much in the visible region for HTP hence the intermolecular interactions between the sub-units (any many body effects) are not affecting the curve in visible region. Yet phase

transition related structural change is related to additional absorption with maximum in green that originates from intermolecular interactions between sub-units in LTP structure.

Density of states

Density of states, **Figure S14**, shows contribution from atomic states to molecular orbitals. The HOMO levels are predominantly located on Br lone pairs, while the LUMO-β has mixed Cu/Br character. Noticeably higher in energy the LUMO-α is localized on H atoms (from amino groups) with small partial Cu character. Comparison between the aligned DOS of N±1 electron systems (energy shifted by $|\Delta|$ = 1.69 eV, **Figure S15)**, shows that around chemical potential energy (corresponding to Fermi level) a state with Cu/Br mixed character appears. This mixed state is LUMO of cationic system (with major contribution from Br) and HOMO of anionic system (with major contribution from Cu). Because this state is found slightly below the chemical potential, determined as mid between HOMO and LUMO, intrinsic or possible p-type semiconduction is suggested.

Appendix

The components of first-order hyperpolarizability, β, are defined as [14,15]

$$\beta_i = \beta_{iii} + \frac{1}{3}\sum_{i \neq j}(\beta_{ijj} + \beta_{jij} + \beta_{jji}), \quad i = x,y,z \tag{24}$$

Employing Kleinman symmetry, one obtains [14-19]

$$\beta_x = \beta_{xxx} + \beta_{xyy} + \beta_{xzz} \tag{25}$$

$$\beta_y = \beta_{yyy} + \beta_{yxx} + \beta_{yzz} \tag{26}$$

$$\beta_z = \beta_{zzz} + \beta_{zyy} + \beta_{zxx} \tag{27}$$

The total intrinsic quadratic hyperpolarizability is

$$\beta_{tot} = \left(\beta_x^2 + \beta_y^2 + \beta_z^2\right)^{\frac{1}{2}} \tag{28}$$

The β_{tot} might be determined only theoretically. Experimentally the vector component along the dipole moment direction, can be found:

$$\beta_{vec} = \sum_i \frac{D_i \beta_i}{|D|} \tag{29}$$

The former definitions refer to solution-phase measurements, while for the gas-phase measurements the component parallel to the ground state charge transfer direction is used [15]

$$\beta_{\parallel} = \frac{3}{5}\beta_{vec} \tag{30}$$

The ratio of β_{vec} to β_{tot} gives direction of charge transfer in a molecule [20]

$$\frac{\beta_{vec}}{\beta_{tot}} = cos\theta, \quad \theta: \measuredangle\left(\vec{D}, \vec{\beta}_{vec}\right) \tag{31}$$

The θ is angle between β_{vec} and electric dipole moment, hence if ratio is ±1 the charge transfer is parallel or antiparallel to the molecular dipole moment.

References

1. Koopman's theorem – kohn-Sham version
2. Yang, W.; Parr, R. G., Hardness, softness, and the fukui function in the electronic theory of metals and catalysis, Proc. Nat. Acad. Sci. USA 82 (1985) 6723-6726.
3. Ayers, P.W., The physical basis of the hard/soft acid/base principle, Faraday Discuss., 2007,135, 161-190.
4. Bühl, M.; Kabrede, H., Geometries of Transition-Metal Complexes from Density-Functional Theory, J. Chem. Theory Comput. 2006, 2, 5, 1282–1290.
5. Iron, M.A., Evaluation of the Factors Impacting the Accuracy of 13 C NMR Chemical Shift Predictions using Density Functional Theory-The Advantage of Long-Range Corrected Functionals, J. Chem. Theory Comput. 2017, 13, 5798−5819.
6. Sattler, K., Chapter 2 - The energy gap of clusters, nanoparticles, and quantum dots in Handbook of Thin Films, Vol. 5, Academic Press, 2002, Pages 61-97.
7. Abdullah, B.J., Size effect of band gap in semiconductor nanocrystals and nanostructures from density functional theory within HSE06, MSSP 2022, 137, 106214.
8. Krishnakumar, V.; Nagalakshmi, R., Studies on the first-order hyperpolarizability and terahertz generation in 3-nitroaniline, Physica B: Condensed Matter, 403, 2008, 1863-1869.
9. Heid, E.; Heind, M.; Dienst, P.; Schröder, C., Additive polarizabilities of halides in ionic liquids and organic solvents, J. Chem. Phys. 2018, 149, 044302.

10. Bernardes, C. E. S.; Shimizu, K; Lopes, J. N. C.; Marquetand, P.; Heid, E.; Steinhauser, O.; Schröder, C., Additive polarizabilities in ionic liquids, Phys. Chem. Chem. Phys., 2016,18, 1665-1670.

11. Gagné, O.; Hawthorne, F.; Shannon, R.D.; Fischer, R.X., Empirical electronic polarizabilities: deviations from the additivity rule. I. M2+ SO4·nH2O, blödite Na 2M2+ (SO4)2 ·4H2O, and kieserite-related minerals with sterically strained structures, Phys Chem Minerals (2018) 45:303–310.

12. Miller, K.J., Additivity methods in molecular polarizability, J. Am. Chem. Soc. 1990, 112, 23, 8533–8542.

13. Safi, Z.S.; Wazzan, N., DFT calculations of 1H- and 13C-NMR chemical shifts of 3-methyl-1-phenyl-4-(phenyldiazenyl)-1H-pyrazol-5-amine in solution, Scientific Reports, (2022) 12:17798.

14. Jeewandara , A.K.; de Silva, K.M.N.; Are Donor–Acceptor Self Organised Aromatic Systems NLO (Non-linear Optical) Active?, J. Mol. Struct., 2004, 686, 131–136.

15. Kanis, D.R.; Ratner, M.A.; Marks, T.J.; Design and Construction of Molecular Assemblies with Large Second-Order Optical Nonlinearities. Quantum Chemical Aspects, Chem. Rev., 1994, 94, 195–242.

16. Chattaraj, P.K.; Sengupta, S.; Popular Electronic Structure Principles in a Dynamical Context, J. Phys. Chem. 1996, 100, 16126-16130.

17. Parr, R.G.; Yang, W.; Density-Functional Theory of Atoms and Molecules, Oxford University Press, New York, 1989.

18. Pralok, K.S.; Mehboob, A.Md.; Ramprasad, M.; , Swapan, K.P.; Tuning of hyperpolarizability, and One- and Two-Photon Absorption of Donor–Acceptor and Donor–Acceptor–Acceptor-Type Intramolecular Charge Transfer-Based Sensors, Phys. Chem. Chem. Phys. 2019,21, 17343-17355.

19. Kleinman, D.A.; Nonlinear Dielectric Polarization in Optical Media, Phys. Rev., 1962, 126, 1977.

20. Machado, D.F.S.; Lopes, T.O.; Lima, I.T.; da SilvaFilho, D.T.A.; de Oliveira, H.C.B.; Strong Solvent Effects on the Nonlinear Optical Properties of Z and E Isomers from Azo-Enaminone Derivatives, J. Phys. Chem. C 2016, 120, 17660–17669.